A&A 568, A98 (2014)
DOI: 10.1051/0004-6361/201423504

Astronomy & Astrophysics

Herschel view of the large-scale structure in the Chamaeleon dark clouds⋆

C. Alves de Oliveira[1], N. Schneider[2,3], B. Merín[1], T. Prusti[4], Á. Ribas[1,5,6], N. L. J. Cox[7], R. Vavrek[1], V. Könyves[8,9], D. Arzoumanian[9], E. Puga[1,10], G. L. Pilbratt[4], Á. Kóspál[4], Ph. André[8], P. Didelon[8], A. Men'shchikov[8], P. Royer[7], C. Waelkens[7], S. Bontemps[2,3], E. Winston[4], and L. Spezzi[11]

[1] European Space Agency (ESA/ESAC, SRE-O), PO Box 78, 28691 Villanueva de la Cañada, Madrid, Spain
e-mail: calves@sciops.esa.int
[2] Université de Bordeaux, Laboratoire d'Astrophysique de Bordeaux, CNRS/INSU, 33270 Floirac, France
[3] CNRS, LAB, UMR 5804, 33270, Floirac, France
[4] European Space Agency (ESA/ESTEC, SRE-S), Keplerlaan 1, 2201 AZ Noordwijk, The Netherlands
[5] Ingeniería y Servicios Aeroespaciales, European Space Agency (ESA/ESAC, SRE-O), PO Box 78, 28691 Villanueva de la Cañada, Madrid, Spain
[6] Centro de Astrobiologia (INTA-CSIC), PO Box 78, 28691 Villanueva de la Cañada, Madrid, Spain
[7] Instituut voor Sterrenkunde, KU Leuven, Celestijnenlaan 200D, bus 2401, 3001 Leuven, Belgium
[8] Laboratoire AIM, CEA/DSM-CNRS-Université Paris Diderot, IRFU/SAp, CEA Saclay, Orme des Merisiers, 91191 Gif-sur-Yvette, France
[9] IAS, CNRS (UMR 8617), Université Paris-Sud 11, Bâtiment 121, 91400 Orsay, France
[10] Vega, European Space Agency (ESA/ESAC, SRE-O), PO Box 78, 28691, Villanueva de la Cañada, Madrid, Spain
[11] European Southern Observatory (ESO), Karl-Schwarzschild-Strasse 2, 85748 Garching bei München, Germany

Received 24 January 2014 / Accepted 23 April 2014

ABSTRACT

Context. The Chamaeleon molecular cloud complex is one of the nearest star-forming sites and encompasses three molecular clouds (Cha I, II, and III) that have a different star-formation history, from quiescent (Cha III) to actively forming stars (Cha II), and one that reaches the end of star-formation (Cha I).
Aims. We aim at characterising the large-scale structure of the three sub-regions of the Chamaeleon molecular cloud complex by analysing new far-infrared images taken with the *Herschel* Space Observatory.
Methods. We derived column density and temperature maps using PACS and SPIRE observations from the *Herschel* Gould Belt Survey and applied several tools, such as filament tracing, power-spectra, Δ-variance, and probability distribution functions (PDFs) of the column density, to derive the physical properties.
Results. The column density maps reveal a different morphological appearance for each of the three clouds, with a ridge-like structure for Cha I, a clump-dominated regime for Cha II, and an intricate filamentary network for Cha III. The filament width is measured to be about 0.12 ± 0.04 pc in the three clouds, and the filaments are found to be gravitationally unstable in Cha I and II, but mostly subcritical in Cha III. Faint filaments (*striations*) are prominent in Cha I and are mostly aligned with the large-scale magnetic field. The PDFs of all regions show a lognormal distribution at low column densities. For higher densities, the PDF of Cha I shows a turnover indicative of an extended higher density component and culminates in a power-law tail. Cha II shows a power-law tail with a slope characteristic of gravity. The PDF of Cha III can be best fit by a single lognormal.
Conclusions. The turbulence properties of the three regions are found to be similar, pointing towards a scenario where the clouds are impacted by large-scale processes. The magnetic field might possibly play an important role for the star formation efficiency in the Chamaeleon clouds if it can be proven that it can effectively channel material onto Cha I, and possibly Cha II, but this is probably less efficient on the quiescent Cha III cloud.

Key words. ISM: clouds – ISM: individual objects: Chamaeleon

1. Introduction

Molecular clouds in the Galaxy have a complex spatial structure that is highlighted by the unprecedented sensitivity and resolution of the *Herschel* Space Observatory (Pilbratt et al. 2010) imaging observations, mainly from large survey programs (André et al. 2010; Motte et al. 2010; Molinari et al. 2010). The recent advance in the census of starless and prestellar cores makes it possible to study their connection to the large-scale structure of molecular clouds. Observations show that the prestellar cores identified with *Herschel* are preferentially found within gravitationally unstable filaments (e.g., André et al. 2010, 2014; Polychroni et al. 2013; Könyves et al. 2010; Könyves et al., in prep.) while massive protostellar dense cores and star clusters tend to be found at the junctions of dense filaments (e.g., Hennemann et al. 2012; Schneider et al. 2012; Peretto et al. 2013). The observed orientation of the filaments suggests that they are aligned with the magnetic field (e.g., in the massive star-forming region DR21, Schneider et al. 2010). Recently,

⋆ *Herschel* is an ESA space observatory with science instruments provided by the European-led Principal Investigator consortia and with important participation from NASA.

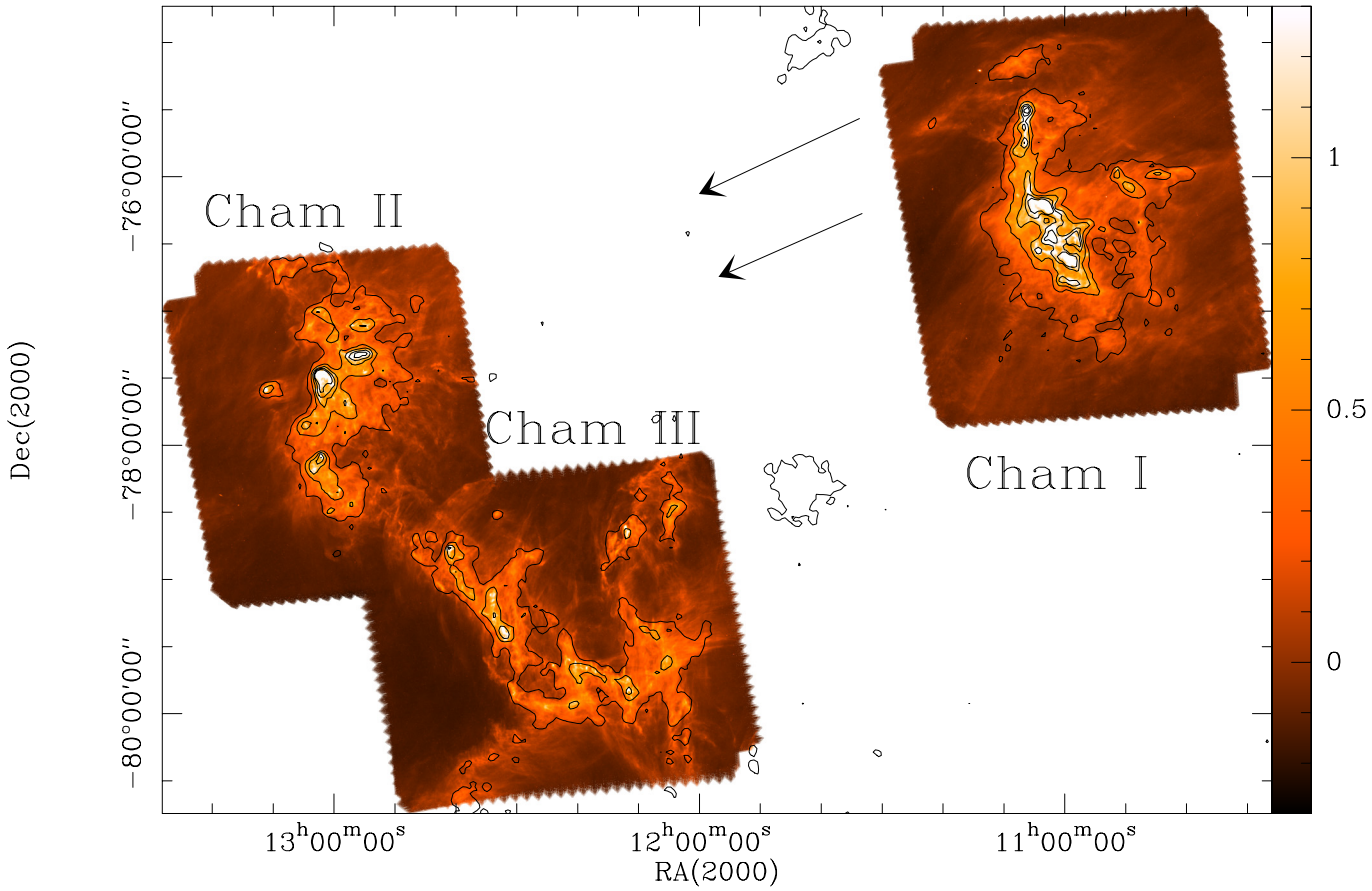

Fig. 1. SPIRE 250 μm map with extinction contours (Schneider et al. 2011) overlaid from 2 to 10 mag, in steps of 2 mag. The arrows show the general orientation of the magnetic field as measured in Cha I by Whittet et al. (1994) and McGregor et al. (1994). Note the preferential alignment of the faint *striations* in Cha I, which are less evident in Cha II or Cha III, where the surrounding diffuse emission takes a variety of orientations. In the region eastwards of Cha III, no *striations* are detected in the *Herschel* maps.

Palmeirim et al. (2013) discovered that low-density filaments (*striations*) in the Taurus region are also preferentially oriented along the magnetic field. These findings suggest that the initial conditions that favour star formation are closely linked to the spatial structure of a molecular cloud. Identifying the processes responsible for the fragmentation of clouds into dense filaments and their subsequent evolution is therefore paramount to understanding core formation and ultimately the dependence of core and stellar masses on the large-scale properties of the interstellar medium.

The Chamaeleon molecular cloud complex is one of the nearest star-forming sites and is located at a distance of 150−180 pc (Whittet et al. 1997). It contains the Cha I, II, and III (Fig. 1) as well as the Musca clouds (Cox et al., in prep.). Mizuno et al. (2001) showed in their ^{12}CO (1→0) survey that the complex is spatially and kinematically coherent with emission in the range of −4 to 6 km s^{-1}. Cha I is the most active star-forming region with a young stellar population of more than ∼200 members (Luhman 2008; Winston et al. 2012) with a median age of ∼2 Myr. Cha II (∼4 Myr) has a smaller population of ∼60 young stellar objects (YSOs; Spezzi et al. 2008, 2013), and no YSO has been found in Cha III (Belloche et al. 2011b). Using the Large APEX Bolometer Camera (LABOCA), Belloche et al. (2011b,a) mapped the dust continuum emission at 870 μm in Cha I and III to single out the possible causes of such different star formation activity. In Cha I, the low number of candidate prestellar cores and protostars and the high global star formation efficiency were interpreted as signs that star formation might be at its end in this cluster, whereas in Cha III evidence for the on-set of star formation was found.

The Chamaeleon dark clouds were observed with *Herschel* as part of the Gould Belt survey (hereafter, HGBS, André et al. 2010). These observations are presented in Sect. 2 and represent an homogeneous dataset in the far-IR across a large area of the cloud complex, which allows us to characterise the large-scale structure and extended emission of the three clouds to better understand their different star formation history. In Sect. 3, we present the different analysis tools employed, such as filament tracing, power spectra, Δ-variance, and probability distribution functions (PDFs) of the column density. The properties derived, such as filamentary vs. clumpy structure, level of turbulence and energy injection, and density structure are presented in Sect. 4 and discussed in Sect. 5, with the conclusions presented in Sect. 6.

2. Observations

The Cha I (obsIDs 1342213178, 1342213179), Cha II (obsIDs 1342213180, 1342213181), and Cha III (obsIDs 1342213208, 1342213209) clouds were observed on the 22 and 23 of January 2011 with the PACS (Poglitsch et al. 2010) and SPIRE (Griffin et al. 2010) instruments onboard *Herschel* in parallel mode with a scanning speed of 60″ s^{-1}. The angular resolutions for PACS at 160 and SPIRE at 250, 350, and 500 μm are ∼12″, ∼18″, ∼25″, and ∼37″, respectively. The PACS maps at 70 μm reveal several point sources but do not contain information on extended

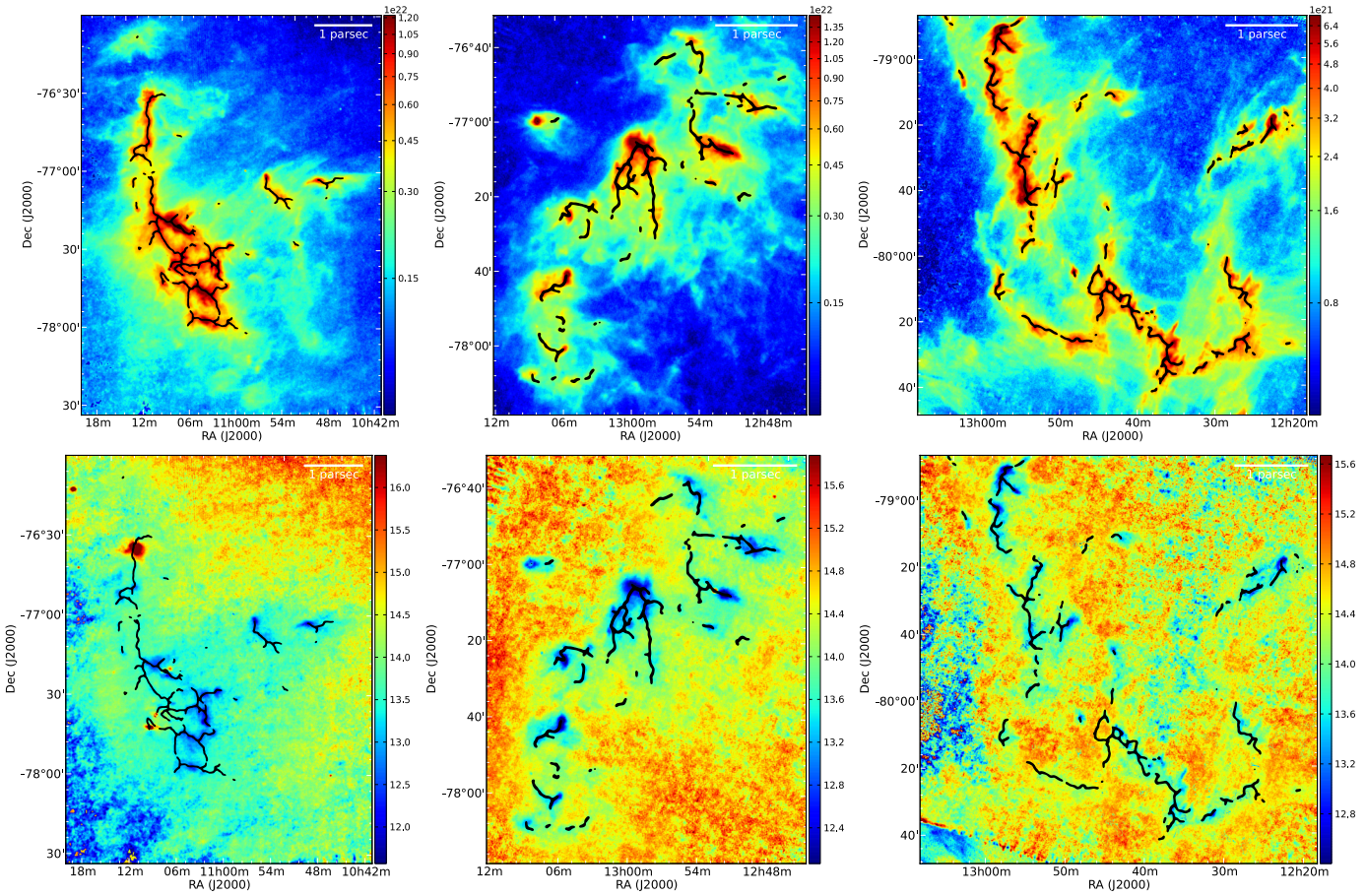

Fig. 2. Column density (N_{H_2}(cm^{-2}), *top*) and temperature (K, *bottom*) maps of Cha I, II, and III (*from left to right*) with the skeletons tracing the most prominent filamentary structure superimposed in black.

emission arising from cold dust, and therefore have not been used in this paper.

We reduced the PACS data with *scanamorphos* version 12 (Roussel 2013), which is described in Winston et al. (2012) and Spezzi et al. (2013). The SPIRE data were reduced within the *Herschel* Interactive Processing Environment (HIPE version 7.2, Ott 2010), using a modified version of the pipeline scripts that includes observations taken during the turnaround at the map borders. The two orthogonally scanned maps were combined using the averaging algorithm "naive-mapper".

3. Methods

In the following, we briefly describe the data analysis procedures and tools used to study the *Herschel* observations. Detailed explanations of each method are given in the cited references.

3.1. Column density and temperature maps

The column density and temperature maps were determined from a modified blackbody fit to the 160, 250, 350, and 500 μm images reprojected on a common 6″/pixel grid, following the procedure detailed in Könyves et al. (2010). The zero-offsets, determined from comparison with *Planck* and IRAS data (Bernard et al. 2010), were first applied to each band. For the region covered by PACS and SPIRE simultaneously, we adopted the same opacity law as in earlier HGBS papers (Könyves et al. 2010), fixing the specific dust opacity per unit mass (dust+gas) to be the power-law $\kappa_\nu = 0.1\ (\nu/1000\ \mathrm{GHz})^\beta$ cm^2/g with $\beta = 2$ (e.g., Hildebrand 1983), and leaving the dust temperature and column density as free parameters. The final error on the column density is statistical (spectral energy density (SED) fitting, photometry) and systematic (opacity law). A recent study by Roy et al. (2014) concluded that the dust opacity law adopted by HGBS is good to better than 50% accuracy in the whole range of column densities between $\sim 3 \times 10^{21}$ and 10^{23} cm^{-2}. Figure 2 shows the resulting maps for the three regions[1].

3.2. Filamentary structure

We used the DisPerSe algorithm (Sousbie 2011; Sousbie et al. 2011) to trace the crest of the filamentary structure of the clouds, using the curvelet component (Starck et al. 2003) of the column density map as an input. This method has been successful in mapping the filamentary network in other regions observed with *Herschel*, and the details can be found, for example, in Arzoumanian et al. (2011) or Schneider et al. (2012). The structure obtained by requiring a persistence threshold of 5×10^{20} cm^{-2} ($\sim 5\sigma$, see Sousbie 2011, for the formal definition of "persistence") in the curvelet image is overlaid on the column density maps shown in Fig. 2. It should be noted that the filamentary structure displayed is derived from the column density map, which is a 2D-projection of the volume density. Since

[1] The column density and temperature maps for Chamaeleon I, II and III can be retrieved from the HGBS archives webpage: http://gouldbelt-herschel.cea.fr/archives

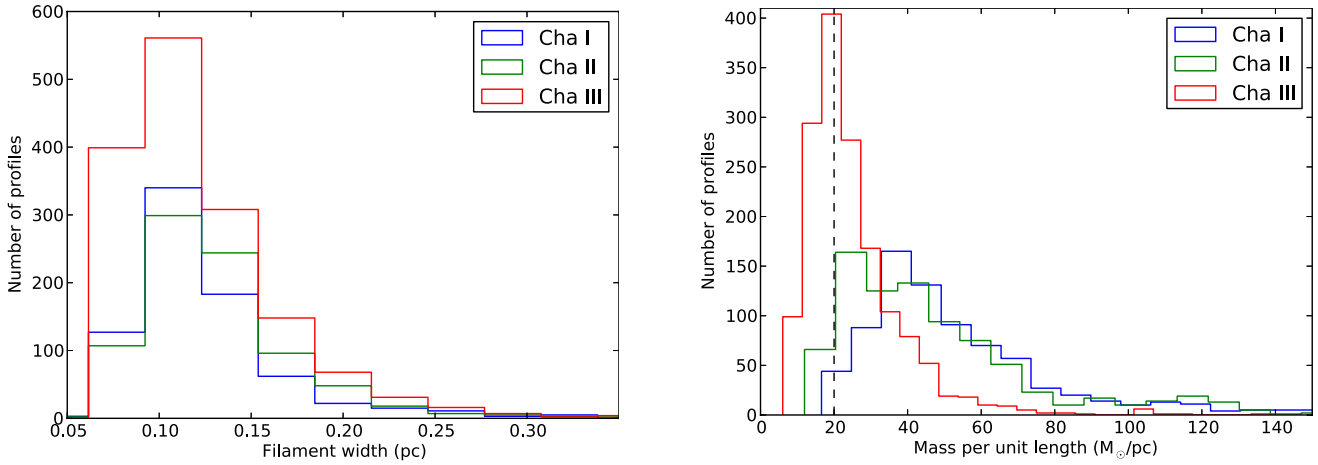

Fig. 3. Distribution of the width (*left*) and mass per unit length (*right*) for individual profiles, as derived for Cha I (blue), Cha II (green), and Cha III (red). In the mass-per-unit-length histogram, the dashed line shows the thermal critical mass per unit length for a gas temperature of ∼12 K.

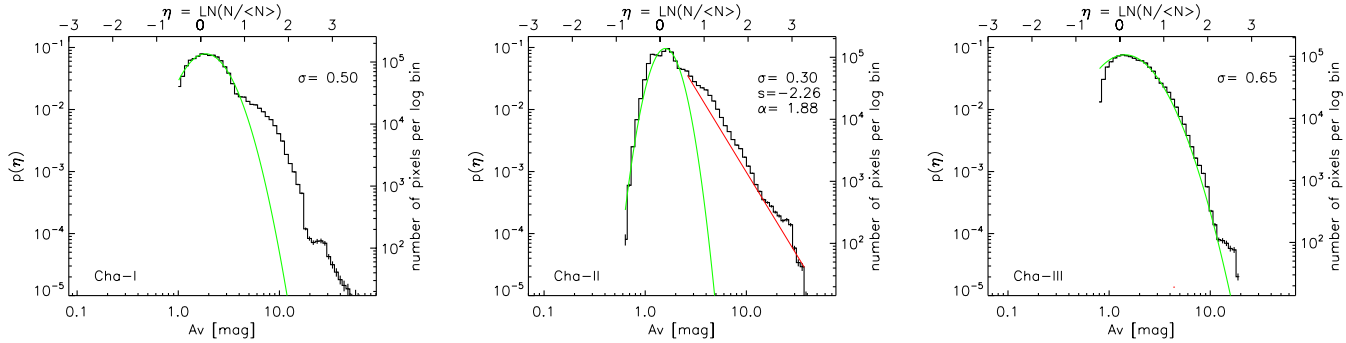

Fig. 4. Probability distribution functions of the column density for the Cha I, II, and III cloud regions. The PDFs were obtained from the column density maps (Fig. 2) at an angular resolution of 36″. The left y-axis indicates the normalised probability and the right y-axis the number of pixels per log bin. The green line indicates the fitted PDF and the red line (in Cha II) the power-law fit to the high-density tail. The width of the PDF (σ), the fitted slope s, and the corresponding exponent α of a spherical density distribution are given in each panel.

DisPerSE works topologically, it connects all emission features such that projection effects may create links between filaments that are not physically related. However, the high spatial resolution of the *Herschel* maps in nearby regions largely alleviates these effects. For example, André et al. (2014; see their Fig. 2) highlighted the good agreement between the fine structure of the *Herschel* column density filaments and the $C^{18}O$ results of Hacar et al. (2013) for Taurus B211/B213.

We characterised the identified filamentary structures by deriving the radial column density profile perpendicular to the tangential direction to the filament crest. The centre of each profile was fitted with a *Gaussian*, from which the FWHM and area were taken to determine the filament width and the mass per unit length (Fig. 3).

3.3. Probability distribution functions of the column density

Probability distribution functions of the (column) density characterise the fraction of gas with a column density N in the range [N, N+ΔN]. For the Chamaeleon clouds, the PDFs are represented by the distribution of the number of pixels per log bin versus the column density, expressed in visual extinction (Fig. 4). They are widely used both in observational (e.g., Kainulainen et al. 2009; Schneider et al. 2012, 2013) and numerical (e.g., Federrath & Klessen 2012, and references therein) studies of the (column) density structure of molecular clouds. For example, Klessen (2000) showed that isothermal, hydrodynamic turbulence simulations produce perfectly lognormal PDFs, and PDFs obtained from extinction maps (Lombardi et al. 2008; Kainulainen et al. 2009; Froebrich & Rowles 2010) are lognormal for low extinctions. However, *Herschel* observations of the Polaris cloud (Men'shchikov et al. 2010; Miville-Deschênes et al. 2010) show that even in a clearly turbulence-dominated cloud, the PDF is not simply lognormal but starts to show excess at higher extinctions (Schneider et al. 2013). Though gravity, in general, plays an important role in organising the density structure of a cloud (see below), in a very low density cloud such as Polaris, the excess seen in the PDF can also be due to intermittency. Non-isothermal flows can cause a power-law tail in the PDF (Passot & Vázquez-Semadeni 1998), but we suspect that neither in Polaris nor in the Chamaeleon clouds the temperature difference (only a few K) is enough to provoke such flows. The most dominant process to influence the PDF is thus gravity, where large-scale collapse as well as individual core-collapse determine the density structure and give rise to the observed power-law tail (see, e.g., numerical simulations by Ballesteros-Paredes et al. 2011; Kritsuk et al. 2013; Girichidis et al. 2014). In addition, recent studies (Schneider et al. 2012; Rivera-Ingraham et al. 2013; and Tremblin et al. 2014) showed that radiative feedback processes can have a strong impact as well, leading to double peaks in the PDF and a two-step power law in the tail. The role of the magnetic field is not yet clear, however. Magnetohydrodynamic (MHD) simulations showed that magnetic fields cause a more filamentary density structure

Table 1. Column density and mass values.

Cloud	N_{noise} (1)	N_{max} (2)	$\langle N \rangle$ (3)	Mass (4)
Cha I	0.30	7.26	1.83	865
Cha II	0.31	4.35	1.59	502
Cha III	0.30	1.86	1.25	241

Notes. Columns 1−3: rms noise, peak, average column density in 10^{21} cm^{-2}. Column 4: total mass of the cloud in $M_\odot$ above a threshold of $A_V = 2$ mag ($\approx 2 \times 10^{21}$ cm^{-2}, using the conversion formula $N(H_2)/A_V = 0.94 \times 10^{21}$ cm^{-2} mag^{-1} Bohlin et al. 1978). A distance of 180 pc was taken for Cha I and II, and 150 pc for Cha III.

(Hennebelle 2013) and a narrower PDF (e.g., Federrath et al. 2010). Observationally, a variation on the width of PDFs due to a magnetic field has not yet been observed (e.g., Schneider et al. 2013).

Probability distribution functions are an important tool to distinguish these various processes. To first order, the density PDF is proportional to the column density PDF (Brunt et al. 2010). Ballesteros-Paredes et al. (2011) showed that PDFs vary during cloud evolution, with purely lognormal shapes found in an initially turbulent, non-gravitating cloud, while one or more lognormal PDFs at low column-densities and a power-law tail for higher values were found for later stages of cloud evolution. Fitting the slope of the high-density tail of the PDF (Federrath et al. 2011; Girichidis et al. 2014) enables the computation of the exponent α of the spherical density distribution $\rho(r) = \rho_0 \, (r/r_0)^{-\alpha}$ and thus the relative contribution of turbulence and gravitation in a cloud. In the standard inside-out collapse model of a singular isothermal sphere (Shu et al. 1987), $\alpha = 2$ is consistent with the collapse of a centrally condensed sphere such as a pre-stellar core, while $\alpha = 1.5$ applies to collapsing protostars, that is, it includes envelope collapse. In any case, a value of α between 1.5 and 2 indicates free-fall collapse of individual cores/protostars and/or and ensemble of cores, as was shown in the analytic study of the link between PDF and self-gravity by Girichidis et al. (2014). However, it is not (yet) analytically possible to differentiate in the slope of the power-law tail between local, small-scale core/envelope collapse and larger scale, global collapse of clumps and filaments.

3.4. Power spectra and Δ-variance

To characterise the turbulent structures in the Chamaeleon clouds, we derived scaling relations such as the power spectrum and the Δ-variance[2] (Ossenkopf et al. 2008a,b) for each column density map to measure the relative structural variation as a function of the size scale. The power spectrum $P(k)$ of a 2D image characterises the injection of energy depending on the wavenumber (spatial frequency) k with $P(k) \propto |k|^{\gamma}$. A power-law fit to $P(k)$ gives the slope γ. The Δ-variance (σ_Δ) is directly linked to the power spectrum by $\sigma^2_\Delta \propto L^{\beta-2}$, where $\gamma = 1 - \beta$ and L is the scale size (Stutzki et al. 1998). Fitting the slope provides a measure for the amount of structure on various scales in a given image. A dominance of small-scale structure thus implies a steep slope and high values for β, while large-scale structures cause flat Δ-variance curves. The Δ-variance is determined purely in the spatial domain and thus limits edge-effect problems using Fourier-transform methods, such as power-spectra. It effectively separates real structure from observational artefacts since it uses the error map as a weight, and it is only limited by the spatial resolution and extent of the map. The effect of applying the Δ-variance to 2D projections of a 3D structure (in this case, the *Herschel* column density maps) has been addressed by Mac Low & Ossenkopf (2000), who demonstrated that there is a simple translation between a projected Δ-variance and a 3D Δ-variance.

[2] IDL-based routine *deltavarwidget* provided by V. Ossenkopf, available at www.astro.uni-koeln.de/~ossk/ftpspace/deltavar

4. Results

4.1. Column density and temperature maps

A comparison between the *Herschel* column density map (Fig. 2) and the near-IR extinction map (Schneider et al. 2011) shows the consistency in both structure and intensity (the highest column density is $\sim 7 \times 10^{21}$ cm^{-2} for Cha I, see Table 1). The detailed spatial structure is different for the three clouds. Cha I is dominated by a central *ridge* of emission, that is, an elongated cloud structure of somewhat higher density, surrounded by faint *striations*, which is reminiscent of those found in the B211/3 filament in Taurus by Palmeirim et al. (2013). These cold (11−13 K) features are also clearly seen in the SPIRE 250 μm map (Fig. 1). A comparison with $C^{18}O$ 1→0 data (see Fig. 2 in Haikala et al. 2005) shows that the structures seen in the column density map consist of overlapping filaments that are coherent in velocity, and individual clumps. The only hot spot in all regions is the dust ring around HD 97300 located in Cha I, with $T \sim 25$ K (Kóspál et al. 2012). Cha II has a more fragmented appearance (best seen in Fig. 2) with extended emission regions. In the temperature maps, individual *clumps* are easily identified as patchy, cold (11−14 K) regions. The most clearly defined *filamentary* region (high aspect ratio of the identified structures) is Cha III. Here as well as in the other regions, the cold denser regions are embedded in a lower density ($1-3 \times 10^{21}$ cm^{-2}) background.

The total masses derived from the column density maps are given in Table 1. The values are lower than those estimated from ^{12}CO (1→0) observations (Mizuno et al. 2001) by factors of 1.2, 3.8, and 7.8 for Cha I, II, and III, respectively, and we attribute the discrepancy mainly to the unreliable $^{12}CO/H_2$ conversion factor. The *Herschel*-derived mass for Cha I of 865 $M_\odot$ is higher than that calculated from $C^{18}O$ (1 → 0) data (230 $M_\odot$, Haikala et al. 2005). This difference has been noted by Belloche et al. (2011b), who showed that $C^{18}O$ (1 → 0) is a poor gas tracer below $A_V = 6$ mag. It is nevertheless a reliable tracer of mass between $A_V = 6-15$ mag in Cha I when compared with the mass derived from extinction maps (Belloche et al. 2011b). Furthermore, the region surveyed in Haikala et al. (2005) does not include the western part of Cha I. Our mass estimate agrees with the value derived from the near-IR extinction map (Schneider et al. 2011).

4.2. Filament parameters

The distributions of widths are shown in Fig. 3 (left) for the profiles of the structure traced by the DisPerSe algorithm where the contrast (ratio of the column density at the crest to local background) was >3. This threshold ensures a sufficient number of profiles while minimising contamination from profiles in confused regions. The obtained distributions have a median value $0.115^{+0.038}_{-0.023}$, $0.124^{+0.044}_{-0.029}$, and $0.112^{+0.047}_{-0.026}$ pc (the upper and lower bounds mark the 68% confidence interval) for Cha I, II, and III, respectively. This result shows that there is no significant difference in width between the clouds and agrees with

the characteristic width measured in other star formation regions (e.g., Arzoumanian et al. 2011).

In Fig. 3 (*right*), we show the distribution of the projected mass per unit length for the same profiles. If we take the gas temperature in the Chamaeleon complex filamentary-like structures to be approximately 12 K, the thermal critical mass per unit length is ~20 $M_\odot$/pc. Gravitationally supercritical filaments are defined as having a mass per unit length higher than this critical value. This implies that most of the structures in Cha I and II are supercritical and likely to be undergoing collapse, while in Cha III the majority of the individual profiles where the filaments were probed were found to be subcritical.

4.3. Probability distribution functions of the column density

The PDFs of the column density obtained for the three clouds are displayed in Fig. 4. A lognormal distribution for low extinctions with a width of 0.48 to 0.6 mag and a peak at $A_V \sim 2$ mag is common to the three regions. The PDFs show significant differences for higher column densities.

The PDF for Cha I shows a turnover from a lognormal low-density component into a higher density feature around $A_V = 4-5$ mag. The pixel distribution above these A_V values is neither a power-law tail nor a second lognormal PDF (fitting this component with a lognormal distribution is not possible although it may appear as such by eye-inspection). This scenario resembles that observed in the intermediate/high-mass star-forming region Vela C (Hill et al. 2011) where the same characteristics in the column density map and PDF were attributed to the contrast between a dense and massive ridge, embedded in a lower density gas component. It is therefore possible that the segregation between ridge/bulk emission of a cloud is a common feature in molecular clouds. At even higher column densities ($A_V > 20$ mag) there is a small but significant pixel statistics in the PDF that resembles a power law. Spatially, these pixels comprise the star-forming clumps (see also Sect. 5.2).

The PDF of Cha II shows the clearest example of a power-law tail (although there is some excess in the distribution) starting at $A_V \sim 3$ mag. Fitting a single power-law leads to a slope of $s = -2.26$. Assuming that the power-law tail is due to purely spherical collapse, the density distribution varies as $\rho(r) \propto r^{-\alpha}$, determined from s with $\alpha = -2/s + 1$ (Federrath & Klessen 2013; Schneider et al. 2013), and the exponent α is estimated to be 1.88, which implies the dominance of self-gravity.

The PDF of Cha III can be best fitted by a single lognormal across the whole density range, although the low column density range (left of the peak) is not perfectly covered. Some excess at higher column-densities ($A_V > 10$ mag) is observed, and this feature is now more common in 'quiescent' molecular clouds such as in Polaris (Schneider et al. 2013), or the Spider molecular cloud (Schneider et al., in prep.); it indicates a scenario where these clouds are not only dominated by turbulence (which would lead to a perfectly lognormal PDF). For Polaris, it was argued that statistical density fluctuations and intermittency might cause this excess. In Cha III, however, there are first signs of core formation in some filaments so that we speculate that gravity might cause the start of a power-law tail distribution.

4.4. Power-spectra and Δ-variance

Figure 5 shows the power spectra and Δ-variance for the three clouds. As mentioned in Sect. 3.3, the modulations in the power-spectra are generally less obvious than those in the Δ-variance, therefore we focus the discussion on the latter.

The Δ-variance of Cha I shows a clear change in slope at 0.15 pc, remains flat until ~0.6 pc, and rises again to 2 pc. We interpret this curve as caused by *cores and clumps* (with a size distribution between 0.2 and 0.5 pc, i.e., not determined by turbulence), and by the *ridge* in which the second peak originates. The density distribution seen in the PDFs (Sect. 4.3) is thus also traced in the spatial structure.

In Cha II, the Δ-variance appears to be turbulence dominated (no range of a flat Δ-variance spectrum as for Cha I) but displays a peak at ~0.5 pc that is most likely caused by the typical size scales of the *clumps*, since much fewer *cores* are detected in Cha II, embedded in the larger extended ridge-like structure on a size scale of ~2 pc (second peak).

Finally, Cha III shows a Δ-variance with one peak at ~0.7 pc, probably indicating the typical lengths of the filaments, but appears otherwise to be featureless, consistent with the lack of prominent structures other than the filamentary network.

We note that there is no indication for a typical size scale of 0.1 pc that would represent the filament width. Instead, the constant rise of the curves until the first peak in the different regions indicates that structures on many size scales are present. We assume that in particular the *striations* with their large variation in size prevent a clear identification of filament width for the Δ-variance. The fitted slope of the Δ-variance up to 0.15 pc (lowest common scale until a turnover occurs) gives values of $\beta = 2.49 \pm 0.59$ for Cha I, $\beta = 2.50 \pm 0.21$ for Cha II, and $\beta = 2.36 \pm 0.23$ for Cha III. These values are at the lower end of those found for a large compilation of different molecular clouds by Bensch et al. (2001) and Schneider et al. (2011). The low values indicate that the power is contained in the largest scales, suggesting that large-scale physical processes govern the structure formation in the Chamaeleon complex. These could be an overall magnetic field or energy injection from supernova explosions.

5. Discussion

5.1. Comparison with numerical simulations

To compare our results with turbulence models, we independently computed the hydrodynamic Mach-number ($\mathcal{M}$) using molecular line data (see Schneider et al. 2013; Pineda et al. 2008, for details). In contrast to Belloche et al. (2011b), where $C^{18}O$ $1 \rightarrow 0$ observations were used, we opted for the ^{12}CO $(1 \rightarrow 0)$ data from Mizuno et al. (2001) with the molecular line FWHM between 2 and 2.8 km s^{-1}, since only this line traces the low-density gas component and thus the bulk of the molecular cloud. In the calculation we assumed LTE and additionally that the gas and dust are thermally coupled, taking the maximum brightness temperature at the peak of the line to be the dust temperature derived from our *Herschel* maps (~14 K). Given these assumptions, we caution that the Mach number calculation carries a large uncertainty. We derived values of $\mathcal{M} = 7.2$, 10.0, and 9.3 for Cha I, II, and III, respectively.

A comparison between the observed PDFs and hydrodynamic simulations including gravity, different turbulent states with a range of Mach-number between 2–50 and star formation efficiencies (SFE) from 0 to 20% (Federrath & Klessen 2012) results in fits to models where $\mathcal{M} = 3$, 5, or 10 with solenoidal or mixed forcing (with or without magnetic field) and low SFE. Furthermore, the case of Cha III (mostly lognormal, showing only a slight deviation at high densities, although not a clear power-tail) is only reproduced by an SFE

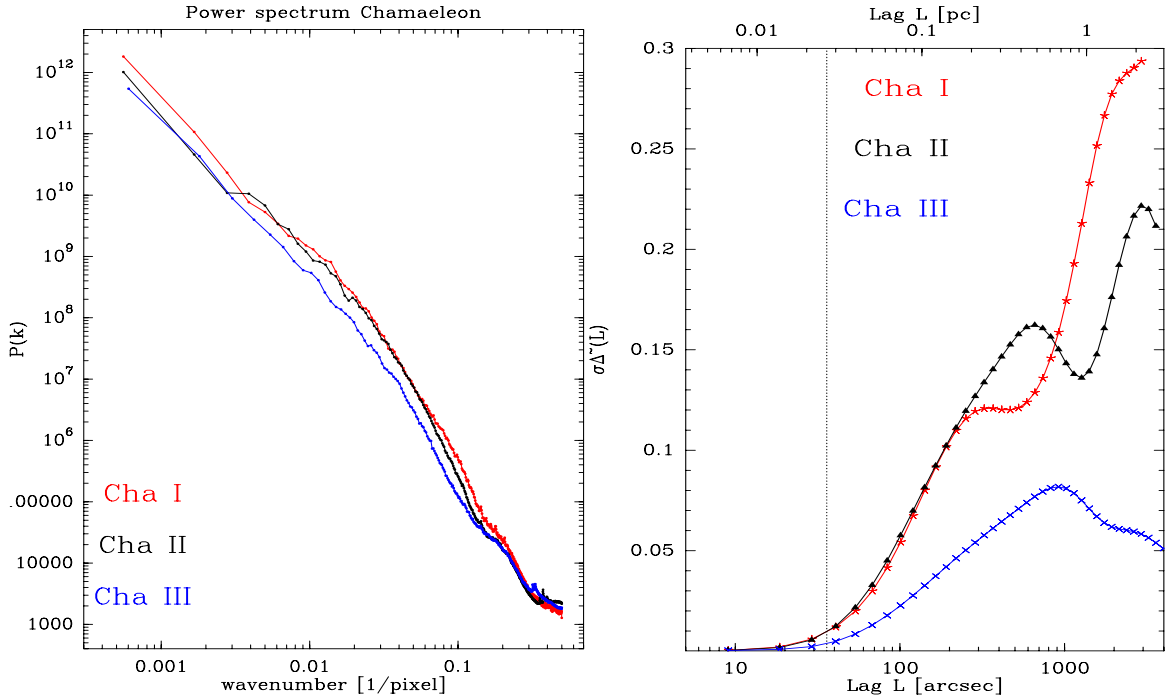

Fig. 5. *Left*: power spectra of the column density maps of the Chamaeleon clouds, which were determined from the *Herschel* images reprojected to a common 6″/pixel grid (see Sect. 3.1). *Right*: the Δ-variance spectra of the same column density maps. The dotted vertical line indicates the resolution limit of 36″.

of 0% and different values of the Mach-number (the higher $\mathcal{M}$, the broader the PDF). The Cha II region cannot be clearly pinpointed. Various combinations of $\mathcal{M}$ and SFE lead to this PDF shape. However, they share the fact that the SFE is higher than 0% and that compressive forcing is not the dominating source of energy because the PDF is narrow. Here, we make use of the results of the Δ-variance that led to slope values of $\beta = 2.3{-}2.5$ (with an error of 0.2 to 0.6) for all regions, corresponding to an $\gamma = -1.3$ to -1.5 for the exponent of the radial density distribution. Comparing these values with Table 2 in Federrath & Klessen (2013) shows that the SFE for these values lies between 0 and 1%. The value of $\alpha = 0$ given in Federrath & Klessen (2013), which was determined from the extinction map presented in Schneider et al. (2011), is consistent with our values, considering our large error on β. The case of Cha I is only vaguely reproduced in some models (e.g., solenoidal forcing with SFE 5% and $\mathcal{M} = 10$) where a cut-off at high densities due to resolution effects may also play a role.

5.2. Peculiar density distribution in Cha I

If our interpretation of a distinct, second (high)-density component for Cha I is correct, the origin of this component remains to be understood. Various authors proposed that the star formation process is close to an end in Cha I (e.g., Belloche et al. 2011b). Our *Herschel* observations show that the region mainly consists of individual dense ($A_V > 10$ mag) cores and clumps (size scales 0.2 to 0.5 pc) embedded in a ridge of emission on a level of $A_V = 4{-}5$ mag with a sharp border to the low-density regime that consists of *striations* (see Figs. 1 and 6, where the ridge is clearly outlined by the $A_V = 4$ mag contour). At this stage of evolution of the Cha I cloud, mass transport to the ridge via *striations* probably does not play a significant role if the star formation process has indeed come to an end, in contrast to the Taurus B211 filament, where Palmeirim et al. (2013)

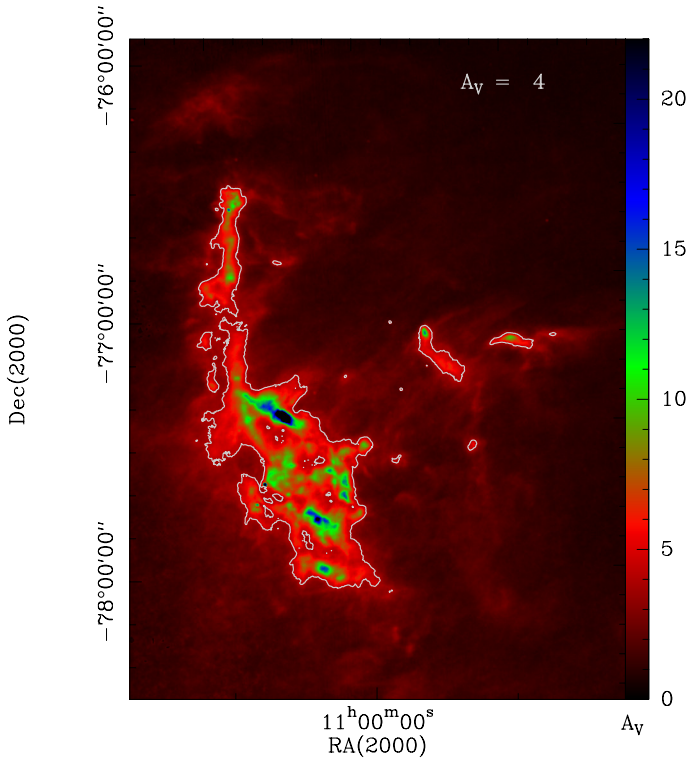

Fig. 6. Column density map of Cha I in which the colour scale is chosen to represent the characteristic A_V levels (4, 10, and ~20 mag) seen in the PDF. The $A_V = 4$ mag level is indicated as a grey contour, while the other two levels become obvious as a change in colour.

argued for mass supply to filaments. The faint *striations* seen in Cha I may be the left-over low-density gas, mixed with dust, aligned with the magnetic field lines (Whittet et al. 1994, see Sect. 5.3). Kainulainen et al. (2011) proposed that such a sharp

spatial/density transition between a ridge and extended emission may be explained by pressure equilibrium. The authors interpreted the deviation of several observed PDFs from a lognormal – turbulence-dominated – distribution at $A_V \approx 4$ as a phase transition between a dense population of clumps and the diffuse interclump medium. This implies that for Cha I the whole ridge should be pressure confined with $\langle N_{\rm ridge}\rangle\langle T_{\rm ridge}\rangle \approx \langle N_{\rm ext}\rangle\langle T_{\rm ext}\rangle$ (assuming equal areas). However, the average external column density ($\langle N\rangle$) is at least a factor of 2 lower than that in the ridge, while the temperatures do not differ much ($T_{\rm ridge} \sim 12$ K and $T_{\rm ext} \sim 13$ K, clearly seen in the *striations*, and up to 14 K at a few pc distance). Pressure confinement would require much higher temperatures, which is not observed.

5.3. Star formation history in the Chamaeleon clouds

In the following, and taking into account the ensemble of parameters extracted from the new *Herschel* observations and previous studies of the Chamaelon clouds, we summarise the information on the star formation history across the three clouds. Cha I has formed stars (clustered in the three Cederblad groups) and shows indications that it has arrived at the end of its star formation. This molecular cloud forms a ridge with a few filamentary structures and clumps. The ridge is embedded in low-density gas with *striations* that run parallel to the magnetic field. Cha II has a clumpy structure with ongoing star-formation, and faint *striations* are only marginally observed. Cha III shows no clear signs of star formation; it is organised into a complex network of filaments with low column densities and shows fewer structures that resemble *striations*. These are particularly absent in the eastern part of the cloud.

If the three clouds are part of a coherent complex (very likely in view of the ^{12}CO data), the question arises why they evolved in a different way. It is proposed by theory that molecular cloud formation is governed by large-scale turbulence such as expanding shock-fronts generated by supernovae explosions. The Chamaeleon region is indeed exposed to the Sco-Cen OB associations, and their stellar winds and supernovae might have initiated the formation of the clouds, which per se is not a reason why the clouds would end up with different properties because of this energy injection. Different initial distributions of atomic hydrogen and statistical dynamics (as seen in colliding H I flow simulations) might have led to the observed cloud pattern, with filaments in Cha III still evolving either to merge and build up a larger structure or dissolve, and a ridge-structure in Cha I where the same process already came to end.

The magnetic field in the region might also play a significant role in shaping the cloud structure and star formation activity. If we assume that the orientation of the large-scale magnetic field measured for Cha I does not change significantly towards Cha III, the fewer *striations* seen in this cloud do not appear to show a preferred alignment. Preliminary results from *Planck* Galatic observations and MHD simulations indicate an anti-correlation between the measured degree of polarisation and the dispersion of polarisation angles[3]. In Chamaeleon, polarisation measurements from the *Planck* satellite could be particularly relevant to understanding their differences in star formation history. Given that the large-scale turbulent structure of the three clouds does not vary by much across the regions, and because the observed differences in the current density structure arise mainly from gravity, the initial difference in mass accretion along these *striations* – guided by the local magnetic field – might have shaped the star formation history of the three regions. This might explain why Cha III is a quiescent cloud if it has not experienced this mass accretion process.

[3] http://www.rssd.esa.int/index.php?project=PLANCK\&page=47_eslab

6. Conclusions

We presented new *Herschel* photometric observations of the three Chamaeleon clouds (I, II, and III) taken with the PACS and SPIRE instruments in a homogeneous way. They were analysed with a set of tools to quantitatively characterise the large-scale structure and extended dust emission, and to study their possible relation with the accentuated differences seen today amongst the three clouds, with Cha I most likely at the end of star formation, Cha II actively forming stars, and Cha III in a quiescent state.

The column density and temperature maps derived from the *Herschel* data reveal important morphological differences for the three clouds, with a ridge-like structure for Cha I surrounded by faint filaments (*striations*) aligned with the large-scale magnetic field, a clump-dominated regime for Cha II, and a complex low-density filamentary network for Cha III.

The filamentary-like structures share a common width ($\sim$0.12 $\pm$ 0.04 pc) consistent with values inferred from observations of other star forming regions (e.g., Arzoumanian et al. 2011; André et al. 2014). However, only in Cha I and II are the filaments found to be predominately gravitationally unstable.

All regions show a PDF described by a lognormal distribution for low column densities with a width of $\sim$0.45 to 0.6 mag and a peak at $A_V \sim 2$ mag. For higher column densities, the PDFs show significant differences, with Cha II being the only region where a classical single power-law tail with a slope indicative of free-fall collapse is seen. We compared the PDFs with the results from hydrodynamic simulations of Federrath & Klessen (2012) and concluded that they are adequately described by models where $\mathcal{M} = 3$, 5, or 10 with solenoidal or mixed forcing (with or without a magnetic field) and low SFE.

Overall, the turbulence properties of the three regions do not show large differences, which supports a scenario where the clouds are impacted by common large-scale processes. We emphasise, however, that an alignment of faint filaments peripheral to dense structures with the magnetic field is clearly seen in Cha I. Similar preferential distributions have been found in other star-forming regions (e.g., Palmeirim et al. 2013). Future results from the *Planck* mission on polarisation will quantify the relation between the magnetic filed and the structures in Cha II and Cha III. If it were proven that *striations* are important channels of accretion of ambient material into filaments, the magnetic field might play an important role in shaping the differences in the star formation history of the Chamaeleon complex regions.

Acknowledgements. We thank the referee for a helpful review. We acknowledge support from the Faculty of the European Space Astronomy Centre (ESAC/ESA). We thank Arnaud Belloche and Pedro Palmeirim for their feedback on an earlier draft of this work. V. K. and Ph. A. acknowledge support from the European Research Council under the European Union's Seventh Framework Programme (FP7/2007-2013 – ERC Grant Agreement No. 291294). N.S., S.B., and P.A. acknowledge support by the ANR (Agence Nationale pour la Recherche) project "STARFICH", number ANR-11-BS56-010. N. Schneider acknowledges funding by the DFG-priority program 1573 (ISM-SPP). A.R. is funded by the ESAC Science Operations Division research funds with code SC 1300016149. N.L.J.C. acknowledges support from the Belgian Federal Science Policy Office via the PRODEX Programme of ESA. D.A. acknowledges support by the European Research Council grant MISTIC (ERC-267934). SPIRE has been developed by a consortium of institutes led by Cardiff Univ. (UK) and including Univ. Lethbridge (Canada); NAOC (China); CEA, LAM (France); IFSI, Univ. Padua (Italy); IAC (Spain); Stockholm Observatory

(Sweden); Imperial College London, RAL, UCL-MSSL, UKATC, Univ. Sussex (UK); and Caltech, JPL, NHSC, Univ. Colorado (USA). This development has been supported by national funding agencies: CSA (Canada); NAOC (China); CEA, CNES, CNRS (France); ASI (Italy); MCINN (Spain); SNSB (Sweden); STFC, UKSA (UK); and NASA (USA). PACS has been developed by a consortium of institutes led by MPE (Germany) and including UVIE (Austria); KU Leuven, CSL, IMEC (Belgium); CEA, LAM (France); MPIA (Germany); INAF- IFSI/OAA/OAP/OAT, LENS, SISSA (Italy); IAC (Spain). This development has been supported by the funding agencies BMVIT (Austria), ESA-PRODEX (Belgium), CEA/CNES (France), DLR (Germany), ASI/INAF (Italy), and CICYT/MCYT (Spain).

References

André, P., Men'shchikov, A., Bontemps, S., et al. 2010, A&A, 518, L102
André, P., Di Francesco, J., Ward-Thompson, D., et al. 2014, Protostars and Planets VI, in press [arXiv:1312.6232]
Arzoumanian, D., André, P., Didelon, P., et al. 2011, A&A, 529, L6
Ballesteros-Paredes, J., Vázquez-Semadeni, E., Gazol, A., et al. 2011, MNRAS, 416, 1436
Belloche, A., Parise, B., Schuller, F., et al. 2011a, A&A, 535, A2
Belloche, A., Schuller, F., Parise, B., et al. 2011b, A&A, 527, A145
Bensch, F., Stutzki, J., & Ossenkopf, V. 2001, A&A, 366, 636
Bernard, J.-P., Paradis, D., Marshall, D. J., et al. 2010, A&A, 518, L88
Bohlin, R. C., Savage, B. D., & Drake, J. F. 1978, ApJ, 224, 132
Brunt, C. M., Federrath, C., & Price, D. J. 2010, MNRAS, 405, L56
Federrath, C., & Klessen, R. S. 2012, ApJ, 761, 156
Federrath, C., & Klessen, R. S. 2013, ApJ, 763, 51
Federrath, C., Roman-Duval, J., Klessen, R. S., Schmidt, W., & Mac Low, M.-M. 2010, A&A, 512, A81
Federrath, C., Sur, S., Schleicher, D. R. G., Banerjee, R., & Klessen, R. S. 2011, ApJ, 731, 62
Froebrich, D., & Rowles, J. 2010, MNRAS, 406, 1350
Girichidis, P., Konstandin, L., Whitworth, A. P., & Klessen, R. S. 2014, ApJ, 781, 91
Griffin, M. J., Abergel, A., Abreu, A., et al. 2010, A&A, 518, L3
Hacar, A., Tafalla, M., Kauffmann, J., & Kovács, A. 2013, A&A, 554, A55
Haikala, L. K., Harju, J., Mattila, K., & Toriseva, M. 2005, A&A, 431, 149
Hennebelle, P. 2013, A&A, 556, A153
Hennemann, M., Motte, F., Schneider, N., et al. 2012, A&A, 543, L3
Hildebrand, R. H. 1983, QJRAS, 24, 267
Kainulainen, J., Beuther, H., Henning, T., & Plume, R. 2009, A&A, 508, L35
Kainulainen, J., Beuther, H., Banerjee, R., Federrath, C., & Henning, T. 2011, A&A, 530, A64
Klessen, R. S. 2000, ApJ, 535, 869
Könyves, V., André, P., Men'shchikov, A., et al. 2010, A&A, 518, L106
Kóspál, Á., Prusti, T., Cox, N. L. J., et al. 2012, A&A, 541, A71
Kritsuk, A. G., Lee, C. T., & Norman, M. L. 2013, MNRAS, 436, 3247
Lombardi, M., Lada, C. J., & Alves, J. 2008, A&A, 489, 143
Luhman, K. L. 2008, in Chamaeleon, ed. B. Reipurth, 169
Mac Low, M.-M., & Ossenkopf, V. 2000, A&A, 353, 339
McGregor, P. J., Harrison, T. E., Hough, J. H., & Bailey, J. A. 1994, MNRAS, 267, 755
Men'shchikov, A., André, P., Didelon, P., et al. 2010, A&A, 518, L103
Miville-Deschênes, M.-A., Martin, P. G., Abergel, A., et al. 2010, A&A, 518, L104
Mizuno, A., Yamaguchi, R., Tachihara, K., et al. 2001, PASJ, 53, 1071
Molinari, S., Swinyard, B., Bally, J., et al. 2010, A&A, 518, L100
Motte, F., Zavagno, A., Bontemps, S., et al. 2010, A&A, 518, L77
Ossenkopf, V., Krips, M., & Stutzki, J. 2008a, A&A, 485, 917
Ossenkopf, V., Krips, M., & Stutzki, J. 2008b, A&A, 485, 719
Ott, S. 2010, in Astronomical Data Analysis Software and Systems XIX, eds. Y. Mizumoto, K.-I. Morita, & M. Ohishi, ASP Conf. Ser., 434, 139
Palmeirim, P., André, P., Kirk, J., et al. 2013, A&A, 550, A38
Passot, T., & Vázquez-Semadeni, E. 1998, Phys. Rev. E, 58, 4501
Peretto, N., Fuller, G. A., Duarte-Cabral, A., et al. 2013, A&A, 555, A112
Pilbratt, G. L., Riedinger, J. R., Passvogel, T., et al. 2010, A&A, 518, L1
Pineda, J. E., Caselli, P., & Goodman, A. A. 2008, ApJ, 679, 481
Poglitsch, A., Waelkens, C., Geis, N., et al. 2010, A&A, 518, L2
Polychroni, D., Schisano, E., Elia, D., et al. 2013, ApJ, 777, L33
Rivera-Ingraham, A., Martin, P. G., Polychroni, D., et al. 2013, ApJ, 766, 85
Roussel, H. 2013, PASP, 125, 1126
Roy, A., André, P., Palmeirim, P., et al. 2014, A&A, 562, A138
Schneider, N., Csengeri, T., Bontemps, S., et al. 2010, A&A, 520, A49
Schneider, N., Bontemps, S., Simon, R., et al. 2011, A&A, 529, A1
Schneider, N., Csengeri, T., Hennemann, M., et al. 2012, A&A, 540, L11
Schneider, N., André, P., Könyves, V., et al. 2013, ApJ, 766, L17
Shu, F. H., Adams, F. C., & Lizano, S. 1987, ARA&A, 25, 23
Sousbie, T. 2011, MNRAS, 414, 350
Sousbie, T., Pichon, C., & Kawahara, H. 2011, MNRAS, 414, 384
Spezzi, L., Alcalá, J. M., Covino, E., et al. 2008, ApJ, 680, 1295
Spezzi, L., Cox, N. L. J., Prusti, T., et al. 2013, A&A, 555, A71
Starck, J. L., Donoho, D. L., & Candès, E. J. 2003, A&A, 398, 785
Stutzki, J., Bensch, F., Heithausen, A., Ossenkopf, V., & Zielinsky, M. 1998, A&A, 336, 697
Whittet, D. C. B., Gerakines, P. A., Carkner, A. L., et al. 1994, MNRAS, 268, 1
Whittet, D. C. B., Prusti, T., Franco, G. A. P., et al. 1997, A&A, 327, 1194
Winston, E., Cox, N. L. J., Prusti, T., et al. 2012, A&A, 545, A145